Moisture-induced cracking in a flexural bilayer with application to historical paintings

E. Bosco[1]*, A.S.J. Suiker[1], N.A. Fleck[2]

[1] Department of the Built Environment,
Eindhoven University of Technology, P.O. Box 513,
5600 MB Eindhoven, The Netherlands

[2] Department of Engineering, Cambridge Center for Micromechanics,
Cambridge University, Trumpington Street,
Cambridge, CB2 1PZ, U.K.

September 10, 2020

Abstract

Crack channelling in a brittle, flexural bilayer, composed of a coating adhering to a substrate of finite thickness, is addressed for the case of a uniform moisture content (or temperature) variation. The linear remote stress profile may lead to three different fracture mechanisms, which are characterized by the degree to which delamination occurs, and whether this delamination is of finite length, or is unstable and grows without limit. Failure mechanism maps illustrate the dependence of the acting crack channelling mechanism, and the corresponding critical crack channelling stress, upon the stiffness mismatch between the layers and upon the ratio of interfacial toughness to coating toughness. Although the results are applicable to bilayers in a wide range of applications, the study focuses on the prediction of crack channelling in historical paintings. The significance of bending of the bilayer upon crack channelling is explored by comparing the fracture characteristics of the simply-supported, flexural bilayer with those of a rigidly supported bilayer that is constrained against bending. These two bilayer systems are representative of the different framing techniques commonly used for historical paintings, with the simply-supported bilayer reflecting a regular wooden panel that can bend freely, and the rigidly supported bilayer characterizing a wooden panel that does not bend as a result of cradle additions composed of several horizontal members and corresponding orthogonal cross-pieces. Independent of the type of framing technique applied, it is shown that crack channelling with delamination

*Correspondence to: e.bosco@tue.nl

can be avoided in historical paintings when the delamination toughness exceeds about half of the mode I toughness of the paint layer. Under these conditions paint flaking does not occur, which preserves the visual appearance of the painting. The failure maps constructed in this study provide a useful tool for museum conservators to identify acceptable indoor humidity and temperature variations for which crack channelling with delamination remains absent in historical paintings.

keywords: coating-substrate systems, crack channelling, plane-strain delamination, hygral and thermal loading conditions, historical paintings

1 Introduction

The development of surface cracks in coating-substrate systems by variations in moisture or temperature play an important role in a wide range of engineering technologies, such as micro-electronics components [1], thermal barrier coatings [2,3], ceramic multi-layers [4] and road pavements [5]. Due to a difference in the coefficients of hygral (or thermal) expansion of the coating and substrate, internal stresses can arise upon moisture (or temperature) fluctuations. The surface cracks that may be generated by these internal stresses reduce the structural integrity of the bilayer system, and ideally should be avoided.

Surface cracks have also been observed in cultural heritage objects, including historical oak wood cabinets [6, 7] and historical paintings [8, 9]. The present study focuses on the prediction of surface cracks in historical paintings, as driven by indoor climate variations. Historical paintings are composed of layer(s) of paint adhering to a canvas or wooden substrate; environmental changes associated with moisture fluctuations and, to a lesser extent, temperature alterations, may lead to their degradation [10], whereby a common mechanism observed is crack channelling [11]. This cracking pattern is usually denoted as *craquelure*, and has been analysed in a series of studies on panel paintings [12–14].

A channelling crack may deflect at the interface between the paint and the substrate, leading to interfacial delamination. This failure mode has been identified in several art-works, see e.g., [15, 16], and its occurrence due to humidity cycles has been recently investigated in [17, 18]. Unlimited, unstable delamination growth at the paint-substrate interface may lead to spallation or flaking of the paint [19,20]. Despite being unsightly, from the practical perspective crack channelling is not considered to be critical by conservators as long as delamination remains absent. Conversely, channelling cracks with delamination present require immediate precautionary measures, such as consolidation treatments, before paint loss occurs and the visual appearance of the historical painting degrades [21]. An illustrative overview of the three fracture scenarios above is presented in Figure 1, with Figure 1(a) showing a fine network of channelling cracks at the paint surface, Figure 1(b) illustrating a crack that has locally kinked at the paint/substrate interface, resulting into two opposite delaminations, and Figure 1(c) displaying a

delaminating crack that grows without limit, thereby inducing paint flaking. From a mechanics point of

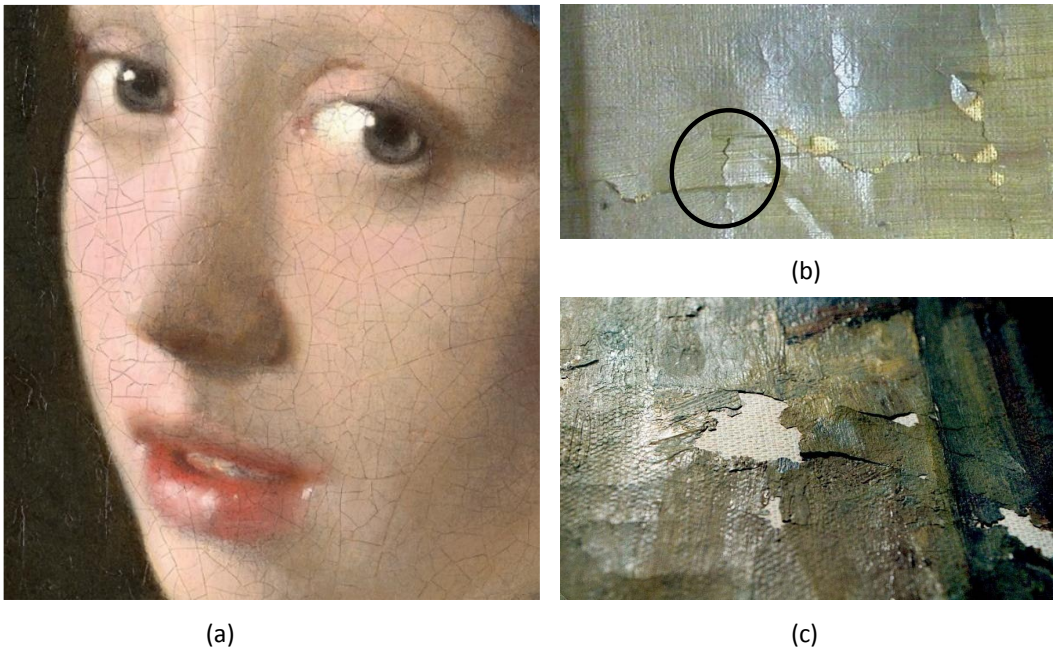

Figure 1: Historical paintings showing an overview of typical fracture mechanisms. (a) *Girl with a Pearl Earring, Johannes Vermeer (ca.1665), Mauritshuis, The Hague.* Fine network of cracks channelling through the paint layer. Picture extracted from [22]; (b) *Still life with flowers, Anonymous Italian, circa 1850, Oil on canvas, Private collection.* Channelling crack that has kinked at the interface between the substrate and the paint layer, thereby introducing two opposite delaminations; (c) *Anonymous Italian, Oil on canvas, Private collection.* Progressive delamination that has led to flaking of the paint material. Pictures (b) and (c) are by courtesy of the photographic archive of Matteo Rossi Doria.

view, these three cracking scenarios may be formally denoted as: *i)* channelling of a mode I crack in the coating with delamination absent (*mechanism 1*), see Figure 2(a), *ii)* channelling of a doubly deflected crack with finite delamination (*mechanism 2*), see Figure 2(b), and *iii)* channelling of a mode I crack with unlimited delamination in all directions (*mechanism 3*), see Figure 2(c). The competition between the three crack channelling mechanisms has been recently explored in [23] by the construction of failure maps. These failure maps summarize the sensitivity of the active crack channelling mechanism, and associated channelling stress, to the ratio of coating toughness to interfacial toughness, to the mismatch in elastic modulus of the layers, and to the mismatch in coefficient of hygral (or thermal) expansion. The study in [23] was performed on a bilayer that was *rigidly supported* in order to impose zero curvature on the system. In this complementary study, the bilayer system is allowed to *bend* by modelling the substrate as *simply-supported*. These two types of support are representative of the different framing techniques used for historical paintings, with the simply-supported bilayer reflecting a regular wooden panel for which out-of-plane bending occurs freely, see Figure 3(a), and the rigidly supported bilayer characterizing a wooden panel that is constrained against out-of-plane bending by cradle additions composed of several

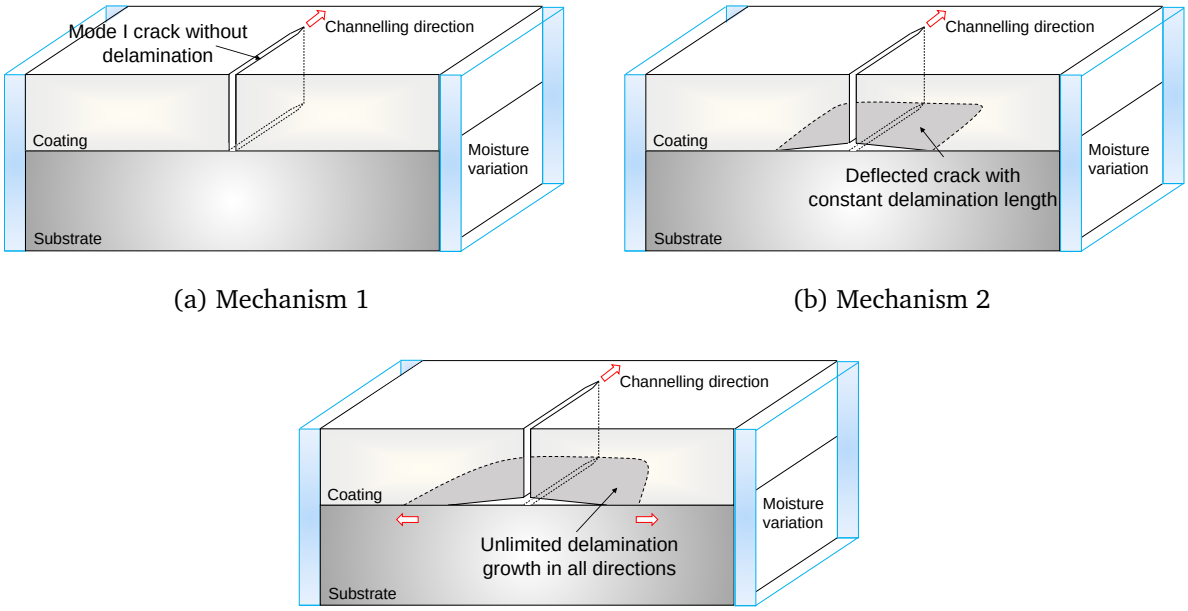

(a) Mechanism 1

(b) Mechanism 2

(c) Mechanism 3

Figure 2: Three possible crack channelling mechanisms for a coating-substrate system consisting of two dissimilar, isotropic hygro-elastic materials and subjected to a uniform change in moisture content. (a) *Mechanism 1*: Channelling of a mode I crack in the coating with delamination absent; (b) *Mechanism 2*: Channelling of a deflected crack with finite delamination length; (c) *Mechanism 3*: Channelling of a mode I crack with unlimited delamination in all directions.

horizontal members and corresponding orthogonal cross-pieces, see Figure 3(b).

In the present study, the aim is to investigate how bending of the bilayer influences the competition between the moisture-induced crack channelling mechanisms sketched in Figure 2, and to determine the critical channelling stress. For this purpose, a brittle crack is analysed that channels in a simply-supported bilayer under a uniform moisture variation. The moisture variation originates from a relative humidity fluctuation, whereby water diffusion is taken to be in steady state, so that time transients do not play a role. As described above, the mode I crack channelling in the coating may kink at the coating-substrate interface into two opposite delaminations of equal length, which results in the doubly deflected crack as depicted in Figure 4. The delamination length can, in principle, exist over the full range of zero to infinity, so that this configuration is representative of all three crack channelling mechanisms that are sketched in Figure 2. The 3D crack channelling mechanisms are investigated by making appropriate use of 2D finite element method results for steady-state crack channelling and plane-strain delamination. The modelling strategy departs from the framework proposed in [23] for the case of moisture-induced channelling cracks in a bilayer that is fully constrained against bending. Comparable modelling strategies have been developed for the analysis of microbuckle tunnelling in fibre composites [25] and crack tunnelling in layered solids [26–28]. The coating and substrate are assumed to be isotropic, linear elastic solids of

(a) Simply-supported wooden panel painting (b) Rigidly supported wooden panel painting

Figure 3: Back view of two panel paintings illustrating different framing techniques. (a) Regular wooden panel (picture courtesy of Paul van Duin). This type of panel painting allows for out-of-plane bending, and may be termed simply-supported. (b) Wooden panel restrained by cradle additions composed of several horizontal members and corresponding orthogonal cross-pieces [24]. This type of panel painting is constrained against out-of-plane bending, and may be termed rigidly supported.

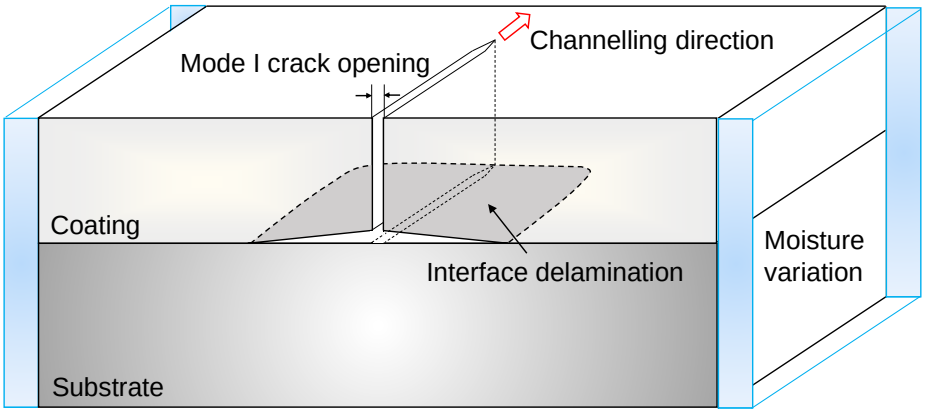

Figure 4: A doubly deflected crack in a brittle elastic coating bonded to an elastic substrate of finite thickness. The crack is generated under a uniform moisture content variation.

differing hygroscopic and stiffness properties. The assumption of elastic isotropy is realistic for the paint material. For an orthotropic substrate made of canvas or wood, this modelling assumption is reasonable if the Young's modulus of the isotropic elastic solid is set equal to the orthotropic stiffness in the direction of the crack face normal [6].

The critical remote stress for steady-state crack channelling is determined from a plane-strain elasticity solution of a doubly deflected crack, whereby the difference in the elastic strain energy upstream and downstream of the channelling crack front is equated to the work of fracture of the doubly deflected crack [25, 27–30]. The delamination toughness is assumed to be constant and independent of the mode-mixity; this assumption is acceptable since the mode-mixity reaches a steady-state value at relatively short delamination lengths for any of the configurations analysed. The numerical results are reduced to failure mechanism maps, which illustrate the operating crack channelling mechanism and the corresponding critical channelling stress as a function of the ratio between the interfacial toughness and mode I toughness of the coating, and the stiffness mismatch between the layers. A comparison of the results for the simply-supported, flexural bilayer with those presented in [23] for a bilayer constrained against bending subsequently reveals the role of bending of the bilayer upon the operating crack channelling mechanism.

The analyses discussed in this work refer to a bilayer subjected to a moisture content variation, but, due to the analogy between moisture diffusion and thermal conduction processes, the results can be directly applied to channelling cracks under thermal fluctuations. In addition, as argued in [23], the surface cracks observed in historical paintings may be treated as isolated defects, since the crack spacing typically exceeds the paint thickness by an order of magnitude, such that interactions become negligible. Although the present study has been inspired by observations of crack formation in historical paintings, the results can be used more generally for applications in which a flexural bilayer may experience channelling cracks under moisture (or temperature) variations.

The paper is organized as follows. The definition of the problem and the governing equations for steady-state crack channelling and plane-strain delamination are presented in Section 2. Section 3 presents the numerical results for crack channelling in a flexural bilayer for which the substrate is of thickness ten times larger that of the coating, since this is representative of historical paintings. Fracture mechanism maps are constructed, and the significance of bending upon the fracture response is determined by comparing the fracture characteristics to those of a bilayer constrained against bending. The main conclusions are reported in Section 4.

2 Problem definition

2.1 Crack geometry and remote layer stresses

Consider a simply-supported bilayer composed of a coating of thickness h_1 bonded to a substrate of thickness h_2, such that the total height equals $h = h_1 + h_2$, see Figure 5. The coating and substrate are isotropic hygro-elastic materials, with Young's moduli E_1 and E_2, Poisson's ratios ν_1 and ν_2 and

hygroscopic coefficients β_1 and β_2, respectively. The system is subjected to plane-strain conditions, and experiences a steady-state hygroscopic loading represented by a uniform[1] moisture content variation across the thickness, $\Delta m(y) = \Delta\bar{m}$.

As illustrated in Figure 5, the moisture content variation may induce tensile stresses in the coating, potentially leading to the growth of a crack-like flaw across the coating thickness that subsequently bifurcates along the coating-substrate interface into two delaminations of length ℓ. The development of the crack and the bending deformation of the bilayer system are described by adopting a Cartesian coordinate system (x, y), with the $x-$axis located at the interface between the coating and the substrate, and the $y-$axis coincident with the end faces of the through-crack in the coating, see Figure 5.

The upstream remote, moisture-induced stresses σ_{xx} in the coating and substrate are represented by $\sigma_1(x \to \infty, y) = \sigma_1^\infty(y)$ and $\sigma_2(x \to \infty, y) = \sigma_2^\infty(y)$, respectively. These stresses can be obtained in closed form by assuming vanishing net force and vanishing net moment across the intact, upstream cross-section, in combination with the compatibility conditions for a coherent coating-substrate interface and the hygro-elastic constitutive laws for the coating and substrate, see Appendix A. Accordingly, the upstream remote stresses in the coating and substrate can be written as

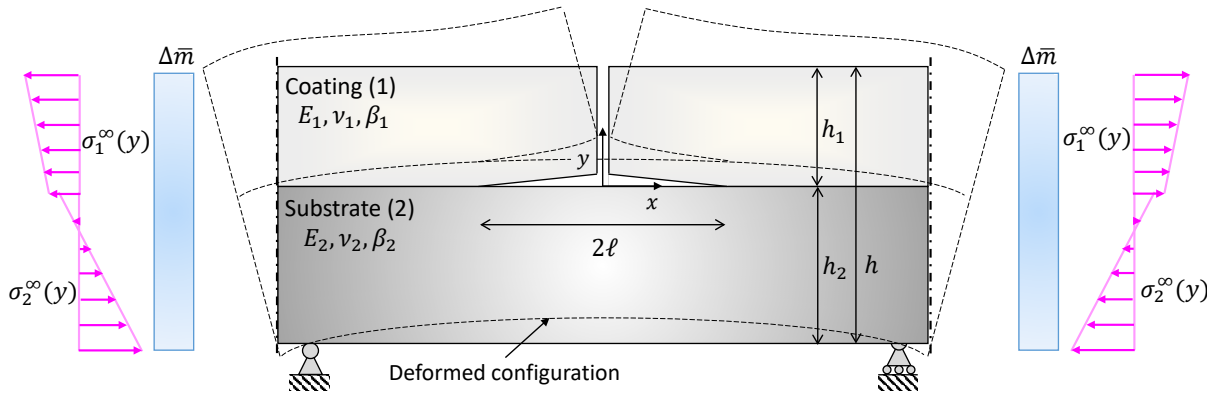

Figure 5: Plane-strain cracking in a bilayer system. Doubly deflected crack at the interface between the coating and substrate due to a uniform change $\Delta\bar{m}$ in moisture content. The bilayer is simply-supported and therefore can bend in-plane. The remote stress profile upstream from the delamination tip depends on the system, the moisture content variation, and the mismatch in hygro-mechanical properties of the individual layers.

$$\begin{aligned} \sigma_1^\infty(y) &= \bar{\sigma}_1 \left(1 - \frac{y}{h\zeta_1}\right) , \\ \sigma_2^\infty(y) &= \bar{\sigma}_2 \left(1 - \frac{y}{h\zeta_2}\right) , \end{aligned} \tag{1}$$

[1]In [23], the fracture response was studied under *uniform* and *linear* moisture content profiles. In the present work, however, the bilayer system is only exposed to a *uniform* moisture content profile. As demonstrated in [23], the fracture responses under uniform and linear moisture profiles are significantly different only when the coating and substrate have a comparable thickness, i.e., $h_2/h_1 \leq 5$; for bilayer systems with a substrate of moderate to large relative thickness, $h_2/h_1 > 5$, the fracture responses under uniform and linear moisture profiles are almost the same.

where

$$\begin{aligned}
\bar{\sigma}_1 &= \frac{\bar{E}_1\bar{E}_2h_2(\bar{\beta}_2-\bar{\beta}_1)(\bar{E}_2h_2^3+3\bar{E}_1h_1^2h_2+4\bar{E}_1h_1^3)}{(\bar{E}_1^2h_1^4+4\bar{E}_1\bar{E}_2h_1^3h_2+6\bar{E}_1\bar{E}_2h_1^2h_2^2+4\bar{E}_1\bar{E}_2h_1h_2^3+\bar{E}_2^2h_2^4)}\Delta\bar{m}\ , \\
\zeta_1 &= \frac{\bar{E}_2h_2^3+3\bar{E}_1h_1^2h_2+4\bar{E}_1h_1^3}{6\bar{E}_1h_1h^2}\ , \\
\bar{\sigma}_2 &= -\frac{h_1}{h_2}\omega\,\bar{\sigma}_1, \\
\zeta_2 &= -\frac{\bar{E}_1h_1}{\bar{E}_2h_2}\omega\,\zeta_1\ ,
\end{aligned} \tag{2}$$

with $\bar{E}_i = E_i/(1-\nu_i^2)$ and $\bar{\beta}_i = \beta_i(1+\nu_i)$ the plane-strain elastic modulus and hygroscopic coefficient of layer i, respectively, where $i=1$ denotes the coating and $i=2$ designates the substrate, and the factor ω is given by

$$\omega = \frac{\bar{E}_1h_1^3+3\bar{E}_2h_2^2h_1+4\bar{E}_2h_2^3}{\bar{E}_2h_2^3+3\bar{E}_1h_1^2h_2+4\bar{E}_1h_1^3}\ . \tag{3}$$

Despite the fact that the applied moisture content variation is uniform, the bilayer bends (with a finite curvature) and a linear stress distribution develops across the thickness of each layer, see Equation (1).

The remote stress σ_1^∞ in the coating, normalized by $\bar{E}_1\bar{\beta}_1\Delta\bar{m}$, is plotted as a function of the relative thickness h_2/h_1 of the bilayer system in Figure 6, with the stress $(1)_1$ evaluated at the interface between the two layers, $\sigma_1^\infty(0) = \bar{\sigma}_1$, and at the top surface of the coating, $\sigma_1^\infty(h_1) = \bar{\sigma}_1(1-h_1/(h\zeta_1))$. The remote stresses are shown for three selected values of stiffness mismatch, $\bar{E}_2/\bar{E}_1 = [0.1, 1, 10]$, and two hygroscopic coefficient mismatches, $\bar{\beta}_2/\bar{\beta}_1 = 0.1$ see Figure 6(a), and $\bar{\beta}_2/\bar{\beta}_1 = 10$ see Figure 6(b). Figure 6(a) shows that both the interface stress $\sigma_1^\infty(0)$ and the top surface stress $\sigma_1^\infty(h_1)$ asymptote to the same compressive stress value with increasing h_2/h_1, and this asymptotic state is independent of the stiffness mismatch $\bar{E}_2/\bar{E}_1$. The stress at the interface, $\sigma_1^\infty(0)$, is unconditionally compressive. Conversely, for stiffness mismatches in the range $0.1 \le \bar{E}_2/\bar{E}_1 \le 1$, the stress at the top surface, $\sigma_1^\infty(h_1)$, is tensile, when the relative thickness h_2/h_1 is lower than a transition value that depends upon $\bar{E}_2/\bar{E}_1$; this is discussed in more detail below. The trends in Figure 6(b) for $\bar{\beta}_2/\bar{\beta}_1 = 10$, are the same as for $\bar{\beta}_2/\bar{\beta}_1 = 0.1$ in Figure 6(a), but with the stress values opposite in sign. Note that the above discussion relates to the case of hygroscopic swelling, which corresponds to a positive moisture content change, $\Delta\overline{m} > 0$. For hygroscopic shrinkage, corresponding to a negative moisture content variation, $\Delta\overline{m} < 0$, the stress σ_1^∞ changes sign, whereby "tension" and "compression" in the discussion above are interchanged. In summary, the coating may experience either a compressive or a tensile stress σ_{xx}, depending on the applied moisture profile, stiffness mismatch, hygroscopic coefficient mismatch and relative substrate thickness.

It is instructive to evaluate the circumstances under which $\sigma_1^\infty(y) > 0$ through the coating, as a tensile stress state promotes crack channelling in the coating. In order for $\sigma_1^\infty(y) > 0$ for $0 \le y \le h_1$, equation

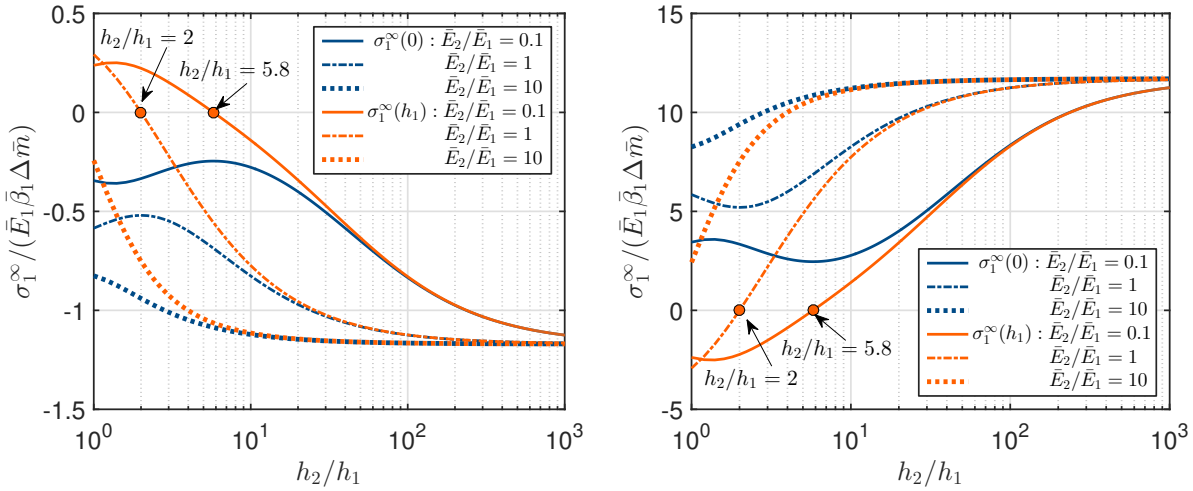

(a) $\bar{\beta}_2/\bar{\beta}_1 = 0.1$ (b) $\bar{\beta}_2/\bar{\beta}_1 = 10$

Figure 6: Stress state in the coating, equation $(1)_1$. Stress value $\sigma_1^\infty(0) = \bar{\sigma}_1$ at the interface between the two layers, and stress value $\sigma_1^\infty(h_1) = \bar{\sigma}_1(1 - h_1/(h\zeta_1))$ at the top surface of the coating, as a function of the relative substrate thickness h_2/h_1, for a hygroscopic coefficient mismatch (a) $\bar{\beta}_2/\bar{\beta}_1 = 0.1$ and (b) $\bar{\beta}_2/\bar{\beta}_1 = 10$. Provided that $\bar{\sigma}_1 > 0$, crack channelling can be activated for a relative substrate thickness $h_2/h_1 \geq 5.8$ for $\bar{E}_2/\bar{E}_1 = 0.1$ and $h_2/h_1 \geq 2.0$ for $\bar{E}_2/\bar{E}_1 = 1$ (as indicated by the dot markers); for $\bar{E}_2/\bar{E}_1 = 10$, crack channelling may occur for arbitrary values of the relative thickness h_2/h_1.

$(1)_1$ demands that

$$\begin{cases} \bar{\sigma}_1 > 0\,, \\ 1 - \dfrac{y}{h\zeta_1} > 0 \qquad \text{for} \qquad 0 \leq y \leq h_1. \end{cases} \tag{4}$$

In the case of hygroscopic swelling, $\Delta\bar{m} > 0$, condition $(4)_1$ is met for a hygroscopic coefficient mismatch $\bar{\beta}_2/\bar{\beta}_1 > 1$, independent of the values of the stiffness mismatch and the relative substrate thickness upon examination of relation $(2)_1$. In contrast, in the case of hygroscopic shrinkage, $\Delta\bar{m} < 0$, the stress in the coating is tensile if $\bar{\beta}_2/\bar{\beta}_1 < 1$. Furthermore, condition $(4)_2$ is met through the coating when it is satisfied at the most critical location, i.e., at the top surface of the coating $y = h_1$. Note from equation $(2)_2$ that condition $(4)_2$ only depends on the elastic and geometrical properties of the bilayer system, and is independent of the hygroscopic coefficient mismatch and the applied moisture content.

The geometrical and material characteristics of the bilayer systems analysed in Section 3 are selected such that the conditions demanded by equation (4) are satisfied. Specifically, the stiffness mismatches between the coating and substrate are taken as $\bar{E}_2/\bar{E}_1 = [0.1, 0.3, 1, 3, 10]$, and the Poisson's ratios of the coating and substrate are assumed to be equal, with $\nu_1 = \nu_2 = 0.3$. In addition, the values for the relative layer thickness h_2/h_1 are selected such that condition $(4)_2$ is satisfied at $y = h_1$. As indicated in Figure 6 by the dots, the transition value for h_2/h_1 above which equation $(4)_2$ is met may depend on the specific value of the stiffness ratio $\bar{E}_2/\bar{E}_1$: for $\bar{E}_2/\bar{E}_1 = 0.1$ and $\bar{E}_2/\bar{E}_1 = 1$, the minimal relative layer thicknesses required for satisfying condition $(4)_2$ are $h_2/h_1 = 5.8$ and $h_2/h_1 = 2$, respectively. For the

highest value of the stiffness mismatch, $\bar{E}_2/\bar{E}_1 = 10$, condition $(4)_2$ holds for any value of the relative thickness ratio h_2/h_1. In summary, for the selection of stiffness mismatches indicated above, condition $(4)_1$ is unconditionally satisfied when the relative thickness ratio $h_2/h_1 \geq 5.8$.

2.2 Steady-state crack channelling with a finite delamination length

The moisture-induced crack channelling mechanisms presented in Figure 2 can be described from the governing equations for the problems of *steady-state crack channelling* and *plane-strain delamination*, which can be derived following the framework presented in [23]. This framework is similar to that established for the analysis of microbuckle tunnelling in fibre composites [25] and for studying crack tunnelling in layered solids [26–28]. The channelling crack in Figure 5 is assumed to have nucleated from an initial crack-like flaw in the coating, and grows as a result of the moisture-induced remote tensile stress $\sigma_1^{\infty}(y)$ given by equation $(1)_1$. During steady-state channelling in the out-of-plane direction of the crack, the channelling front has a constant shape, and the energy release rate does not change with the length of the channelling crack. The energy released per unit advance of channelling crack is obtained from the drop in elastic strain energy ΔW upstream and downstream of the crack channelling front [23, 25, 27–30]; this drop equals the difference between the strain energy stored in an uncracked plane-strain solid and in a cracked plane-strain solid. For the channelling crack with a finite delamination length as illustrated in Figure 5, this energy difference is equal to

$$\Delta W = \frac{1}{2}\int_0^{h_1} \sigma_1^{\infty}(y)\delta(y)\mathrm{d}y \ , \tag{5}$$

where $\delta(y)$ is the relative displacement of the mode I crack faces. Inserting the stress distribution $(1)_1$ into equation (5) leads to

$$\Delta W = \frac{1}{2}\bar{\sigma}_1\bar{\delta}h_1 \ , \tag{6}$$

where $\bar{\sigma}_1$ is the remote coating stress given by equation $(2)_1$ and $\bar{\delta}$ is the average opening displacement across the mode I crack faces, weighted by the factor $1 - y/(h\zeta_1)$, such that

$$\bar{\delta} = \frac{1}{h_1}\int_0^{h_1} \delta(y)\left(1 - \frac{y}{h\zeta_1}\right)\mathrm{d}y \ . \tag{7}$$

Based on dimensional considerations, the average displacement $\bar{\delta}$ defined in expression (7) can be written as

$$\bar{\delta} = \frac{h_1 \bar{\sigma}_1}{\bar{E}_1} f\left(\frac{\ell}{h_1}, \frac{\bar{E}_2}{\bar{E}_1}, \frac{\bar{\beta}_2}{\bar{\beta}_1}\right) , \tag{8}$$

where f is a dimensionless function that depends on the aspect ratio of the crack ℓ/h_1, the stiffness mismatch $\bar{E}_2/\bar{E}_1$ and the hygroscopic coefficient mismatch $\bar{\beta}_2/\bar{\beta}_1$. Upon substituting equation (8) into equation (6), the energy drop per unit crack length ΔW reads

$$\Delta W = \frac{\bar{\sigma}_1^2}{2\bar{E}_1} h_1^2 f\left(\frac{\ell}{h_1}, \frac{\bar{E}_2}{\bar{E}_1}, \frac{\bar{\beta}_2}{\bar{\beta}_1}\right) . \tag{9}$$

Since the elastic energy drop ΔW represents the energy released to form a mode I crack of length h_1 in the coating and two delaminating cracks of length ℓ at the interface, the average energy release rate G_c per unit advance of a channelling crack is obtained from ΔW as [23, 25, 27–30]

$$G_c = \frac{\Delta W}{h_1 + 2\ell} . \tag{10}$$

Now, write Γ_I as the mode I toughness of the coating and Γ_d as the interfacial delamination toughness. Then, the doubly deflected crack can channel if the energy drop ΔW is equal to the work of fracture, which, with equation (10), is expressed by

$$\Delta W = G_c(h_1 + 2\ell) = \Gamma_I h_1 + 2\Gamma_d \ell . \tag{11}$$

The remote coating stress for steady-state channelling, $\bar{\sigma}_1 = \bar{\sigma}_c$, follows by inserting equation (11) into equation (9), to give

$$\bar{\sigma}_c = \left(\frac{2\bar{E}_1 \left(\Gamma_I h_1 + 2\Gamma_d \ell\right)}{h_1^2 f\left(\ell/h_1, \bar{E}_2/\bar{E}_1, \bar{\beta}_2/\bar{\beta}_1\right)}\right)^{\frac{1}{2}} . \tag{12}$$

2.3 Plane-strain crack with a finite delamination length

In the analysis of crack channelling with a finite delamination length, it is necessary to also consider the case of a plane-strain crack across the thickness of the coating with delamination from the crack tip, see Figure 5. For the cracked geometry in Figure 5, the energy release rate for interfacial delamination can be expressed in terms of the energy drop ΔW as given by relation (5), such that

$$G_d = \frac{1}{2} \frac{\partial \Delta W}{\partial \ell} . \tag{13}$$

Here, the factor of 2 relates to the number of delamination tips. In accordance with Griffith's criterion, delamination occurs when the energy release rate G_d equals the delamination toughness Γ_d at the

appropriate mode-mix $\Psi(\hat{l})$, i.e.,

$$G_d = \Gamma_d(\Psi(\hat{l}))\ , \tag{14}$$

with $\hat{l}$ as a reference length that corresponds to the distance ahead of the crack tip at which the mode-mix is evaluated. In order to further specify the function $\Psi(\hat{l})$, consider an interfacial crack between two dissimilar materials, for which the singular stress field at the tip of an interfacial crack is described by a complex stress intensity factor $K = K_1 + iK_2$, where $i = \sqrt{-1}$ and K_1, K_2 are the real and the imaginary parts, respectively, of the stress intensity factor. Following the definition provided in [31, 32], in the asymptotic limit the singular normal σ_{yy} and shear σ_{xy} stress components at a distance r directly ahead of the tip are given by

$$\sigma_{yy} + i\sigma_{xy} = \frac{K}{\sqrt{2\pi r}} r^{i\epsilon}\ , \tag{15}$$

where $r = e^{i\epsilon \ln r} = \cos(\epsilon \ln r) + i\sin(\epsilon \ln r)$, and ϵ is the oscillatory index defined as

$$\epsilon = \frac{1}{2\pi} \ln\left(\frac{1-B}{1+B}\right)\ . \tag{16}$$

Here, B is the second Dundur's elasticity parameter [33]

$$B = \frac{1}{2}\frac{(1-2\nu_2)/G_2 - (1-2\nu_1)/G_1}{(1-\nu_2)/G_2 + (1-\nu_1)/G_1}\ , \tag{17}$$

with $G_j = E_j/(2(1+\nu_j))$ the shear modulus of material $j \in \{1, 2\}$. The classical definition of the phase angle Ψ characterizing the mode-mix equals the ratio between the shear stress and the normal stress on the crack plane immediately ahead of the crack tip. As a consequence of the oscillatory behaviour of the stress field at a bi-material interface this ratio is dependent on the distance r ahead of the crack tip, and thus should be evaluated at an arbitrary, but specified, reference length $\hat{l}$, ahead of the crack tip. Accordingly, the classical definition of the mode-mix needs to be extended to the form [32]

$$\tan(\Psi) = \frac{\sigma_{xy}(r=\hat{l})}{\sigma_{yy}(r=\hat{l})} = \frac{\mathrm{Im}(K\hat{l}^{i\varepsilon})}{\mathrm{Re}(K\hat{l}^{i\varepsilon})}\ . \tag{18}$$

The choice of $\hat{l}$ has only a minor influence on the value of the phase angle Ψ for common values of the oscillatory index $|\epsilon| \ll l$ [32].

Now consider the energy drop ΔW, as defined by expression (9). Upon inserting (9) into (13), the energy release rate G_d per unit advance of delamination follows as

$$G_d = \frac{1}{2}\frac{\partial \Delta W_{\bar{\sigma}}}{\partial \ell} = \frac{\bar{\sigma}_1^2}{4\bar{E}_1} h_1 f'\left(\frac{\ell}{h_1}, \frac{\bar{E}_2}{\bar{E}_1}, \frac{\bar{\beta}_2}{\bar{\beta}_1}\right)\ , \tag{19}$$

where f' is the partial derivative $f' = \partial f/\partial \ell$. The remote coating stress for plane-strain delamination, $\bar{\sigma}_1 = \bar{\sigma}_d$, is calculated by combining equations (19) and (14), giving

$$\bar{\sigma}_d = \left(\frac{4\bar{E}_1 \Gamma_d}{h_1 f'\big(\ell/h_1, \bar{E}_2/\bar{E}_1, \bar{\beta}_2/\bar{\beta}_1\big)} \right)^{\frac{1}{2}} . \tag{20}$$

3 Results

Crack channelling and plane-strain delamination are studied for a simply-supported bilayer system in which the coating and the substrate are characterized by a thickness ratio $h_2/h_1 = 10$. In accordance with the discussion presented in Section 2.1, this thickness ratio guarantees that a tensile remote stress throughout the coating, and consequently one of the crack channelling mechanisms as sketched in Figure 2, may be activated. Furthermore, the choice of $h_2/h_1 = 10$ ensures that the numerical results of the bilayer system can be compared directly with those presented in [23] for a system that is fully constrained against bending, i.e., a bilayer with a rigidly supported substrate, recall Figures 3(a) and 3(b).

3.1 Finite element model

The Finite Element Method (FEM) is used to analyse the cracked configuration of Figure 5; for convenience, the commercial finite element program ABAQUS Standard[2] has been used. The degree of symmetry of the configuration is such that only half of the bilayer system needs to be modelled. Horizontal roller supports are applied over the height of the substrate and at its mid-length to impose the symmetry. In addition, a vertical roller support, applied at the lower right corner of the substrate, prevents rigid body motion and yet allows for in-plane extension/contraction and bending of the system under the applied moisture content variation. The bilayer is taken to be sufficiently long, i.e., $200h_1$, for end effects to be negligible. The fracture response is computed for delamination lengths in the range $\ell/h_1 \in [0.05, 20]$. For each delamination length, a different finite element mesh was employed. The finite element configurations contain 4816 to 14075 plane-strain 8-node quadratic iso-parametric elements, equipped with a 3×3 Gauss quadrature. A preliminary mesh refinement study confirmed that the chosen meshes lead to converged numerical results. At the delamination tip, the square root singularity of the stress field is simulated by moving the mid-side nodes on the crack faces to the 1/4 point nearest to the crack tip. In addition, for each tip element, three neighbouring nodes are collapsed to the crack tip.

As already discussed in Section 2.1, the elastic mismatch between the coating and the substrate is selected as $\bar{E}_2/\bar{E}_1 = [0.1, 0.3, 1, 3, 10]$, and the Poisson's ratios of the two layers are taken to be $\nu_1 = \nu_2 =$

[2]Dassault Systems Simulia Corp, Providence, RI, U.S.A.

0.3. The hygroscopic coefficient mismatch is chosen such that $\bar{\beta}_2 > \bar{\beta}_1$, for which the fracture condition (4) is met if the uniform moisture content applied is positive, $\Delta\bar{m} > 0$, and of sufficient magnitude. The moisture-induced remote stresses for steady-state crack channelling and plane-strain delamination, as given by equations (12) and (20), are determined from the FEM results in accordance with the following procedure.

i) Critical remote stress for steady-state crack channelling: The opening displacement $\delta(y)$ of the crack faces in the coating is extracted from the FEM simulations, and is used to compute the average crack opening displacement $\bar{\delta}$ via relation (7), along with its non-dimensional value f via equation (8). The function f is subsequently used to compute the remote stress $\bar{\sigma}_c$ for crack channelling by means of equation (12).

ii) Critical remote stress for plane-strain delamination: The numerical simulations provide the value of the path-independent J-integral. For a brittle elastic material, the J-integral equals the energy release rate per unit advance of delamination G_d at the delamination tip, i.e., $G_d = J$ [34]. The energy release rate is used to compute the derivative f' through relation (19), which serves as input for the computation of the remote stress $\bar{\sigma}_d$ for plane-strain delamination via equation (20).

The analysis results will be presented by using appropriate dimensionless parameters. Accordingly, the results for the stresses for steady-state crack channelling and plane-strain delamination are applicable for arbitrary values of the hygroscopic coefficient mismatch $\bar{\beta}_2/\bar{\beta}_1$.

3.2 Crack channelling in a simply-supported bilayer

The three crack channelling scenarios depicted in Figure 2 will be first analysed for the flexural, simply-supported bilayer depicted in Figure 5, followed by a comparison of the results with those presented in [23] for a bilayer that is fully constrained against bending, recall Figures 3(a) and 3(b). For all stiffness mismatches considered, the mode-mix computed for the flexural bilayer attains a steady-state value when the delamination length l approaches the coating thickness h_1, with the mode II contribution being slightly more dominant than the mode I contribution. Since the trend is comparable to that of the bilayer constrained against bending, see [23], it will not be displayed here. It follows that, for the calculation of the remote crack channelling stress via equation (12), and of the delamination stress via equation (20), it is reasonable to assume that the delamination toughness Γ_d is constant.

3.2.1 Failure mechanisms

The steady-state crack channelling stress $\bar{\sigma}_c$ and plane-strain delamination stress $\bar{\sigma}_d$ are illustrated in Figures 7(a), (b) and (c) as a function of delamination length ℓ/h_1 for stiffness mismatches $\bar{E}_2/\bar{E}_1 = 0.1$, $\bar{E}_2/\bar{E}_1 = 1$ and $\bar{E}_2/\bar{E}_1 = 10$, respectively. The crack channelling stress $\bar{\sigma}_c$ is calculated as a function

of delamination length ℓ/h_1 from equation (12), and is illustrated by the blue lines for a selection of toughness mismatches $\Gamma_d/\Gamma_I = [0.05, 0.1, 0.2, 0.5, 1, 10]$. The delamination stress $\bar{\sigma}_d$ follows from equation (20) and is designated by the orange line. The crack channelling and delamination stresses are plotted in dimensionless form by applying a normalization by the factor $\sqrt{(\bar{E}_1\Gamma_d)/h_1}$; hence, a crack channelling stress $\bar{\sigma}_c$ related to a larger toughness ratio Γ_d/Γ_I corresponds to a smaller mode I toughness of the coating material. The steady-state stress $\bar{\sigma}_{ss}$ to which the $\bar{\sigma}_c(\ell/h_1)$ and $\bar{\sigma}_d(\ell/h_1)$ curves converge under increasing delamination is obtained analytically, by computing the steady-state energy release rate $G_{ss} = G_d(\ell/h_1 \to \infty)$ from the difference in elastic strain energy upstream and downstream of the delamination tip, and equating the result to the delamination toughness Γ_d, see Appendix B for more details. This leads to the expression

$$\bar{\sigma}_{ss} = \left(2\bar{E}_1\Gamma_d\right)^{\frac{1}{2}} \left(h_1 \left[1 - \frac{h_1}{\zeta_1 h} + \frac{h_1^2}{3\zeta_1^2 h^2} + \omega^2 \frac{\bar{E}_1}{\bar{E}_2}\frac{h_1}{h_2}\left(1 + \frac{h_2}{\zeta_2 h} + \frac{h_2^2}{3\zeta_2^2 h^2}\right)\right]\right)^{-\frac{1}{2}}, \tag{21}$$

with the parameters ζ_1, ζ_2 and ω given by equations $(2)_2$, $(2)_4$ and (3), respectively.

In correspondence with the procedure described in [23, 25–28], the results in Figure 7 allow for an identification of the three crack channelling scenarios sketched in Figure 2 as a function of the toughness ratio Γ_d/Γ_I and the stiffness mismatch $\bar{E}_2/\bar{E}_1$. Consider first Figure 7(a), which presents the $\bar{\sigma}_c(\ell/h_1)$ and $\bar{\sigma}_d(\ell/h_1)$ curves for a stiffness mismatch $\bar{E}_2/\bar{E}_1 = 0.1$. The delamination stress $\bar{\sigma}_d$ follows a monotonically rising branch (R-curve behaviour) that approaches the value of the steady-state stress $\bar{\sigma}_{ss}$ at large delamination lengths. Since stable plane-strain delamination is defined by an increasing stress $\bar{\sigma}_d$ versus delamination length ℓ/h_1, channelling of a doubly deflected crack with finite delamination corresponds to a crack channelling curve intersecting with the *rising branch* of the delamination curve, which occurs for toughness ratios in the range $0.25 \leq \Gamma_d/\Gamma_I < 1.0$. Note that the value of the crack channelling stress at the intersection between the $\bar{\sigma}_c(\ell/h_1)$ curve and the $\bar{\sigma}_d(\ell/h_1)$ curves represents a *minimum* of the $\bar{\sigma}_c(\ell/h_1)$ curve. This can be verified by applying the condition $\partial\bar{\sigma}_c/\partial\ell = 0$ to expression (12) for the crack channelling stress, which leads to $\bar{\sigma}_{c,min} = \bar{\sigma}_d$, with $\bar{\sigma}_d$ given by equation (20). At the intersection point between the two curves the corresponding delamination length ℓ/h_1 can be read off from the horizontal axis of Figure 7(a). In Figure 2 the fracture scenario described above is denoted as *mechanism 2*. Conversely, for relatively small toughness ratios $\Gamma_d/\Gamma_I < 0.25$, the crack channelling stress $\bar{\sigma}_c$ *decreases* monotonically under increasing delamination ℓ/h_1. In this case the critical, *minimum* crack channelling stress coincides with the steady-state value at infinite delamination length, $\bar{\sigma}_{c,min} = \bar{\sigma}_c(\ell/h \to \infty) = \bar{\sigma}_{ss}$. Accordingly, crack channelling is characterized by unlimited delamination growth in all directions, in correspondence with *mechanism 3* illustrated in Figure 2. Finally, for $\Gamma_d/\Gamma_I \geq 1.0$ the crack channelling

curve $\bar{\sigma}_c(\ell/h_1)$ in Figure 7(a) falls completely below the delamination curve $\bar{\sigma}_d(\ell/h_1)$, as a result of which there are no intersection points between the two curves. Consequently, for $\Gamma_d/\Gamma_I \geq 1.0$ delamination remains absent during crack channelling, which is consistent with the observation that the minimum value of the crack channelling curve here occurs at zero delamination, $\ell/h_1 = 0$, see Figure 7(a). In Figure 2 this fracture scenario is referred to as *mechanism 1*.

In summary, from the numerical results presented in Figure 7(a) it can be concluded that crack channelling with delamination absent (*mechanism 1*) operates for toughness ratios in the range $\Gamma_d/\Gamma_I \geq 1.0$, crack channelling with finite delamination (*mechanism 2*) is active for $0.25 \leq \Gamma_d/\Gamma_I < 1.0$, and crack channelling with unlimited delamination growth in all directions (*mechanism 3*) is operational for $\Gamma_d/\Gamma_I < 0.25$. From the value of the minimum crack channelling stress in the coating, $\bar{\sigma}_1 = \bar{\sigma}_{c,min}$, the critical value of the corresponding moisture content variation can be straightforwardly computed via equation $(2)_1$.

Consider now Figure 7(b), which reflects a bilayer system with a stiffness mismatch $\bar{E}_2/\bar{E}_1 = 1$. Note that the crack channelling and delamination curves are qualitatively similar to those presented in Figure 7(a) for $\bar{E}_2/\bar{E}_1 = 0.1$. Mechanism 1, 2 and 3 are active for the respective regimes $\Gamma_d/\Gamma_I \geq 0.44$, $0.32 \leq \Gamma_d/\Gamma_I < 0.44$ and $\Gamma_d/\Gamma_I < 0.32$.

For the choice of stiffness mismatch $\bar{E}_2/\bar{E}_1 = 10$, see Figure 7(c), the delamination curve does not contain an obvious rising part and is approximately horizontal, indicating that *mechanism 2* does not occur. Instead, for toughness ratios $\Gamma_d/\Gamma_I < 0.43$ *mechanism 3* is operational, while *mechanism 1* is active when $\Gamma_d/\Gamma_I \geq 0.43$.

3.2.2 Failure mechanism map

From the identification of the three crack channelling mechanisms as described in Section 3.2.1 above, a failure mechanism map can be constructed in which the minimum crack channelling stress $\bar{\sigma}_{c,min}$ is plotted as a function of the toughness ratio Γ_d/Γ_I for a selection of stiffness mismatches $\bar{E}_2/\bar{E}_1$, see Figure 8. This failure map provides the critical crack channelling stress given the values of the toughness ratio Γ_d/Γ_I and the elastic stiffness mismatch $\bar{E}_2/\bar{E}_1$. The three failure mechanisms are characterized by the regions defined by the dotted orange lines. It can be observed that *mechanism 3* is active, independent of the value of stiffness mismatch, when the toughness ratio is relatively low, i.e., $\Gamma_d/\Gamma_I < 0.25$. Under increasing toughness ratio *mechanism 3* is replaced by *mechanism 2*; the transition between these two failure mechanisms occurs at a slightly larger toughness ratio Γ_d/Γ_I if the stiffness ratio $\bar{E}_2/\bar{E}_1$ is higher. Note that, for a very high stiffness ratio $\bar{E}_2/\bar{E}_1 \geq 10$, *mechanism 2* is never active, and under increasing Γ_d/Γ_I *mechanism 3* switches directly to *mechanism 1*. For $\bar{E}_2/\bar{E}_1 < 10$, *mechanism 2* is active for an

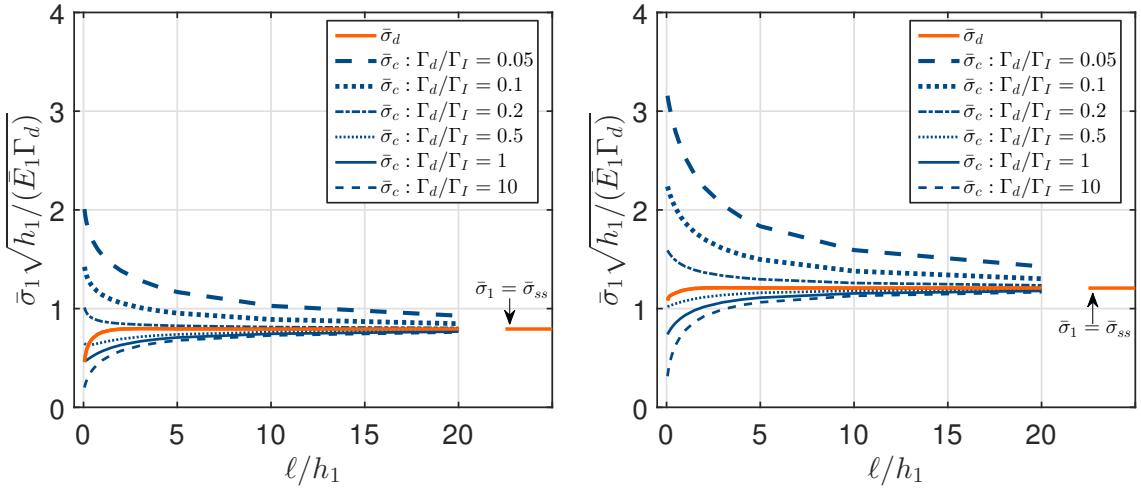

(a) $\bar{E}_2/\bar{E}_1 = 0.1$ (b) $\bar{E}_2/\bar{E}_1 = 1$

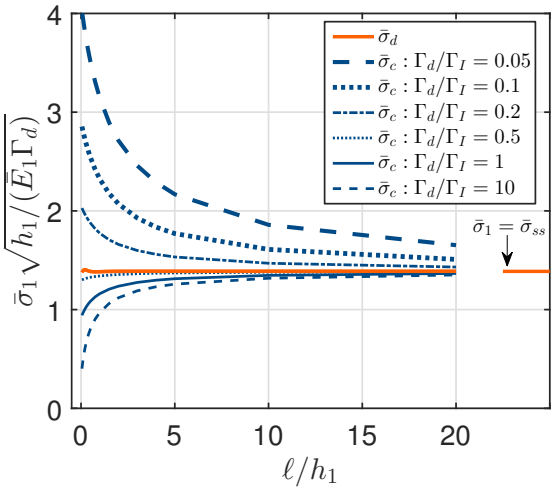

(c) $\bar{E}_2/\bar{E}_1 = 10$

Figure 7: Crack channelling and plane-strain delamination in a simply-supported bilayer with $h_2/h_1 = 10$. Remote stress $\bar{\sigma}_1$ versus delamination length ℓ/h_1 for a stiffness mismatch (a) $\bar{E}_2/\bar{E}_1 = 0.1$, (b) $\bar{E}_2/\bar{E}_1 = 1$ and (c) $\bar{E}_2/\bar{E}_1 = 10$. The blue lines refer to the crack channelling stress $\bar{\sigma}_1 = \bar{\sigma}_c$, equation (12), for selected toughness ratios Γ_d/Γ_I. The orange line represents the plane-strain delamination stress $\bar{\sigma}_1 = \bar{\sigma}_d$, equation (20). The depicted steady-state value $\bar{\sigma}_{ss}$ is calculated with equation (21). The results are independent of the mismatch in the coefficient of hygral expansion, $\bar{\beta}_2/\bar{\beta}_1$.

intermediate range of toughness ratios.

The failure map illustrated in Figure 8 provides a practical tool for determining the fracture susceptibility of historical paintings under indoor climate conditions typically maintained in museums. As an example, consider the panel painting configuration studied in [35], which is composed of a lime wood (*Tilia* species) support and a pictorial layer based on a preparatory ground layer of gesso. Gesso is made of chalk and behaves relatively brittle, by which the pictorial layer is vulnerable to cracking. Since the hygral expansion coefficient of gesso is two orders of magnitude smaller than that of lime wood, $\bar{\beta}_2/\bar{\beta}_1 >> 1$ [13, 35], cracking may occur if the moisture content variation is positive, $\Delta\bar{m} > 0$. In his-

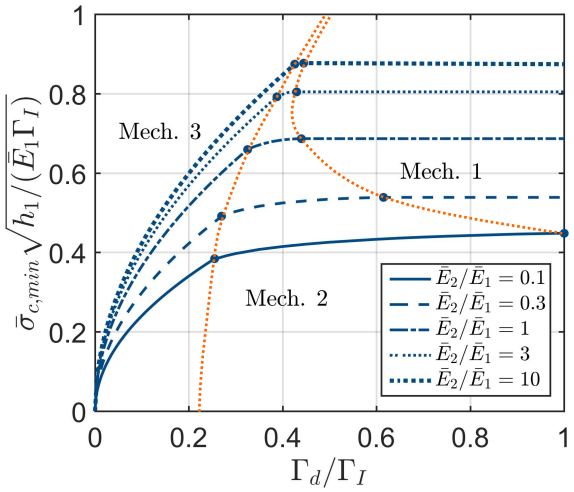

Figure 8: Failure mechanism map for a simply-supported bilayer with $h_2/h_1 = 10$. Minimum channelling stress $\bar{\sigma}_{c,min}$ versus fracture toughness ratio Γ_d/Γ_I for a broad selection of stiffness mismatches $\bar{E}_2/\bar{E}_1$. The dotted orange lines define the regions corresponding to the three failure mechanisms presented in Figure 2. The results are independent of the mismatch in coefficient of hygral expansion, $\bar{\beta}_2/\bar{\beta}_1$.

torical oil paintings the thickness ratio h_2/h_1 between the support and the pictorial layer typically ranges between 5 and 40 [35, 36], so that the value of $h_2/h_1 = 10$ selected for constructing the failure map in Figure 8 may be considered as representative. Using the experimental values of material parameters as reported in [35], crack channelling is first considered with respect to the *tangential* material direction of lime wood, with the stiffness equal to $E_T = 480$ MPa, and the value of the Poisson's ratio as $\nu_{RT} = 0.346$. With these values, the "equivalent isotropic" plane-strain stiffness of lime wood becomes $\bar{E}_2 = 480/(1-0.436^2) = 545$ MPa [3] Additionally, for the gesso the Young's modulus measured at 50% relative humidity (which is representative of the indoor climate conditions applied in museums [7]) equals 7000 MPa, and the Poisson's ratio is $\nu = 0.2$, leading to $\bar{E}_1 = 7000/(1-0.2^2) = 7292$ MPa, and thereby to a stiffness mismatch $\bar{E}_2/\bar{E}_1 \approx 0.1$. The mode I fracture toughness of the gesso reported in [35] was measured from a mode I splitting test on a double cantilever beam specimen composed of a gesso layer sandwiched between two lime wood layers, and equals $\Gamma_I = 100$ N/m. The delamination toughness measured from the same test turned out to have a similar value, $\Gamma_d = 100$ N/m. Although the delamination toughness under the mixed-mode loading conditions representative of crack channelling in a panel painting (see Section 3.2) may be expected to be somewhat larger than the above mode I delamination toughness, as a working assumption the conservative mode I value for the delamination toughness is adopted here, resulting in a toughness ratio $\Gamma_d/\Gamma_I = 1$. The failure mechanism map in Figure 8 illustrates that for the present stiffness and toughness ratios the occurrence of crack channelling in a panel painting is characterized by a transition state from *mechanism 1* to *mechanism 2*. Hence, it can be concluded

[3] The plain-strain stiffness moduli $\bar{E}_1$ and $\bar{E}_2$ selected for computing the results in Figure 8 are based on Poisson's ratios $\nu_1 = \nu_2 = 0.3$. Since the specific value of the Poisson's ratio of a layer may be expected to have a minor influence on the computational results, the failure map in Figure 8 is applicable for bilayers with arbitrary Poisson's ratios.

that the channelling crack propagates without delamination, but that a slight decrease in the toughness ratio will immediately lead to the activation of delamination with a constant length. The corresponding minimum channelling stress can be read off from Figure 8 as $\bar{\sigma}_{c,min} = 0.45\sqrt{(\bar{E}_1\Gamma_I)/h_1}$ which, with the above-mentioned stiffness and toughness values and the thickness of the gesso layer as $h_1 = 1$ mm, results in $\bar{\sigma}_{c,min} = 12.2$ MPa. With the thickness of the lime wood support as $h_2 = 10h_1 = 10$ mm, insertion of the value for the minimum tunnelling stress into equation $(2)_1$ gives $(\bar{\beta}_2 - \bar{\beta}_1)\Delta\bar{m} = 8.3 \times 10^{-3}$. Although this result refers to hygroscopic expansion in terms of a moisture content variation $\Delta\bar{m}$, it may be alternatively expressed in terms of a relative humidity variation ΔRH as $(\bar{\beta}_2^* - \bar{\beta}_1^*)\Delta RH = 8.3 \times 10^{-3}$, with $\bar{\beta}_1^*$ and $\bar{\beta}_2^*$ the hygroscopic coefficients of the painting and substrate per $\%$ of relative humidity change. Inserting the values reported for gesso, $\beta_1^* = 3.2 \times 10^{-6}$ [13], and lime wood (in the tangential material direction), $\beta_2^* = 4.7 \times 10^{-4}$ [35], into this expression leads to a critical relative humidity variation for progressive crack channelling of $\Delta RH = 17.8\%$.

As a next step, crack channelling is considered with respect to the *radial* material direction of lime wood. Adopting the stiffness parameters $E_R = 875$ MPa, $\nu_{RT} = 0.631$, and a hygroscopic coefficient $\beta_2^* = 3.0 \times 10^{-4}$ reported in [35], an analysis similar to the one presented above can be performed. Accordingly, in the radial material direction the stiffness mismatch obtains a two times higher value than in tangential material direction, $\bar{E}_2/\bar{E}_1 = 0.2$, which, in accordance with Figure 8, corresponds to a somewhat higher critical stress of $\bar{\sigma}_{c,min} = 0.5\sqrt{(\bar{E}_1\Gamma_I)/h_1} = 13.6$ MPa for crack channelling under *mechanism 1*. However, due to the relatively low value of the hygroscopic coefficient in the radial material direction, from equation $(2)_1$ the critical relative humidity variation required for generating a progressive channelling crack appears to be lower, i.e., $\Delta RH = 12.5\%$, and therefore is more critical than the value computed above for the tangential material direction.

The practical example above shows that for an orthotropic substrate material it is necessary to determine the critical relative humidity change for crack channelling from analyses in the two *separate* in-plane material directions. Note further that the value of $\Delta RH = 12.5\%$ lies well above the maximal allowable relative humidity variation of $\Delta RH^{max} = 5\%$ applied in the larger international museums for the preservation of their art collection [7], and thus is on the safe side.

3.3 Effect of bending of the bilayer on crack channelling

The effect of bending of the bilayer on crack channelling is studied by comparing the fracture characteristics of the present, simply-supported bilayer, which undergoes bending, with that of the rigidly supported bilayer analysed in [23], which is constrained against bending, recall Figures 3(a) and 3(b), respectively.

3.3.1 Steady-state delamination (*mechanism 3*)

The influence of bending of the bilayer on crack channelling is first demonstrated by considering the stress $\bar{\sigma}_{ss}$ for unlimited, steady-state delamination. As explained in Section 3.2.1, the steady-state delamination stress acts as the minimum crack channelling stress for *mechanism 3* depicted in Figure 2. The steady-state delamination stress for a flexural bilayer is given by expression (21), while for a bilayer without bending it reads [23]

$$\bar{\sigma}_{ss} = \left(2\bar{E}_1\Gamma_d\right)^{\frac{1}{2}} \left(h_1 \left[1 + \frac{\bar{E}_1 h_1}{\bar{E}_2 h_2} \right] \right)^{-\frac{1}{2}} . \tag{22}$$

Note that the critical remote coating stresses (22) and (21) are *independent* of the hygroscopic coefficient mismatch $\bar{\beta}_2/\bar{\beta}_1$. The steady-state stresses (21) and (22) are plotted in Figure 9 as a function the relative layer thickness h_2/h_1 for a selection of stiffness mismatches $\bar{E}_2/\bar{E}_1 = [0.1, 1, 10]$. For the system without bending, the imposed uniform moisture content variation generates a *constant* remote stress in the coating [23]. Accordingly, the only requirement that needs to be satisfied for activating crack channelling is that this remote stress is tensile, i.e., condition $(4)_1$ must be met. Hence, as indicated by the blue lines, the steady-state delamination stress (22) is plotted along the complete range of relative layer thicknesses h_2/h_1 considered in Figure 9. For the flexural bilayer, however, the imposed uniform moisture content variation generates a *linear* remote stress profile across the coating thickness, see equation $(1)_1$. Consequently, to guarantee that crack channelling can occur, *both* the conditions $(4)_1$ and $(4)_2$ need to be satisfied. Since the latter condition is dependent on the stiffness mismatch $\bar{E}_2/\bar{E}_1$ and the relative layer thickness h_2/h_1, the steady-state delamination stress (21) is only valid for a limited range of relative layer thicknesses h_2/h_1 that depends on the value of the stiffness mismatch $\bar{E}_2/\bar{E}_1$, see the orange lines in Figure 9.

It can be further noted from Figure 9 that a higher stiffness ratio $\bar{E}_2/\bar{E}_1$ leads to a higher steady-state delamination stress $\bar{\sigma}_{ss}$, both for the bilayer without bending and the flexural bilayer. Further, under an increasing relative layer thickness h_2/h_1 the steady-state delamination stresses of the two bilayer systems asymptotically converge to the same stress value $\bar{\sigma}_{ss}(h_2/h_1 \to \infty) = \sqrt{2\bar{E}_1\Gamma_d/h_1}$, which is independent of the stiffness mismatch $\bar{E}_2/\bar{E}_1$. This behaviour is consistent with the feature that the bending contribution to the fracture response decreases to zero when the substrate thickness tends to infinity. Note, however, that the shapes of the $\bar{\sigma}_{ss}(h_2/h_1)$ curves of the two bilayer systems are different: for the system without bending the curve is characterised by a monotonic increase towards the asymptotic stress value as mentioned above, while, for the flexural bilayer, the curve first decreases to a minimum, and subsequently increases towards the asymptotic stress value. As a consequence, for a bilayer characterized

by a relatively thin (*thick*) substrate the steady-state delamination stress in the case of bending is larger (*smaller*) than in the case of no bending.

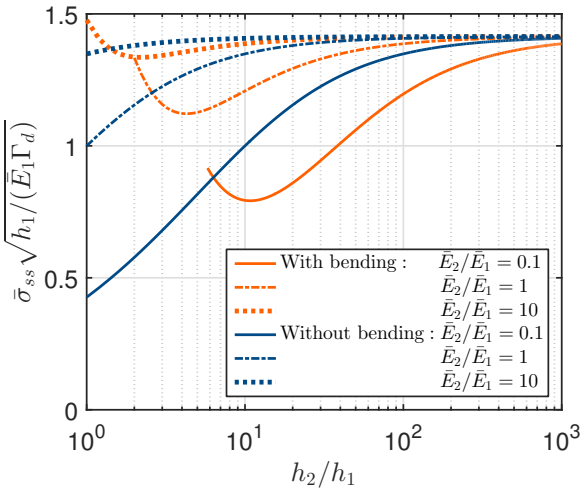

Figure 9: Steady-state stress $\bar{\sigma}_{ss}$ for plane-strain delamination as a function of the relative substrate thickness h_2/h_1 for bilayer systems *with bending* (orange lines), equation (21) and *without bending* (blue lines), equation (22). The results are plotted for a broad selection of stiffness mismatches $\bar{E}_2/\bar{E}_1$, and are independent of the mismatch in coefficient of hygral expansion, $\bar{\beta}_2/\bar{\beta}_1$.

3.3.2 Failure maps for bilayers with and without bending

Figure 10 summarizes the regimes of crack channelling mechanisms of the bilayer as a function of the elastic stiffness mismatch $\bar{E}_2/\bar{E}_1$ and toughness ratio Γ_d/Γ_I. The orange dotted lines delineate the regimes for the flexural bilayer system, which have been constructed based on the results presented in Figure 8. The blue dashed lines characterize the fracture regions for the bilayer system without bending; these results have been taken from [23]. In broad terms, the active regime of *mechanism 2* exists at lower toughness mismatch values Γ_d/Γ_I for the bilayer that is constrained against bending. Note also that at large stiffness ratios $\bar{E}_2/\bar{E}_1 > 3$ the toughness mismatch range for which mechanism 2 is operational becomes relatively small. Independent of the type of substrate support, for a wide range of stiffness mismatches $\bar{E}_2/\bar{E}_1 > 0.5$ crack channelling with delamination is prevented when the delamination toughness exceeds half of the mode I toughness of the coating. This result serves as a general, practical guideline for the prevention of paint delamination in historical paintings.

It is also instructive to display the minimum stresses for *mechanisms 1* and *3* as a function of the stiffness mismatch $\bar{E}_2/\bar{E}_1$ for bilayer systems with and without bending, see Figure 11. The minimum crack channelling stress $\bar{\sigma}_{c,min}$ is normalized by the factor $\sqrt{(\bar{E}_1\Gamma_c)/h_1}$, with $\Gamma_c = \Gamma_I$ in the case of *mechanism 1* (indicated by the solid lines) and $\Gamma_c = \Gamma_d$ in the case of *mechanism 3* (indicated by the dashed lines). Figure 11 may serve as a design graph provided the failure mechanism is known. For the

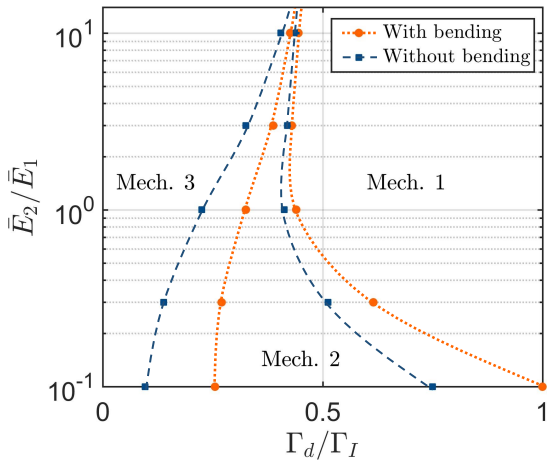

Figure 10: Possible failure mechanisms (depicted in Figure 2) as a function of the elastic mismatch $\bar{E}_2/\bar{E}_1$ and toughness ratio Γ_d/Γ_I for bilayer systems *with bending* (orange dotted lines) and *without bending* (blue dashed lines). The results are computed for a relative layer thickness $h_2/h_1 = 10$, and are independent of the mismatch in coefficient of hygral expansion, $\bar{\beta}_2/\bar{\beta}_1$.

flexural bilayer system the minimum crack channelling stress for *mechanism 1* is calculated by taking the limit $\bar{\sigma}_{c,min} = \bar{\sigma}_c(\ell/h_1 \to 0)$ from the FEM results presented in Section 3.2.2. For the system without bending the results have been taken from [23]. Further, the critical crack channelling stress for *mechanism 3* is obtained from equations (21) and (22) for the systems with and without bending, respectively. Observe that the minimum crack channelling stress generally increases with increasing stiffness ratio $\bar{E}_2/\bar{E}_1$; for *mechanism 1* the curves for the two bilayer systems appear to be close, especially at larger stiffness ratio $\bar{E}_2/\bar{E}_1 > 1$. Conversely, for *mechanism 3* the minimum crack channelling stress turns out to be larger for the system without bending, although the difference in critical stress decreases with increasing stiffness mismatch and vanishes when the substrate becomes infinitely stiff. Finally, note that in Figure 11 *mechanism 2* can intervene, depending on the value of the toughness mismatch Γ_d/Γ_I, as demonstrated by the failure mechanism map depicted in Figure 8.

4 Conclusions

Crack channelling is investigated in a brittle, simply-supported coating-substrate system subjected to a uniform moisture (or temperature) variation. The linear remote stress profile generated under bending of the bilayer may lead to three different fracture mechanisms: $i)$ channelling of a mode I crack in the coating without delamination, $ii)$ channelling of a doubly deflected crack with constant delamination, and $iii)$ channelling of a mode I crack with unstable, unlimited delamination growth in all directions. Failure mechanism maps have been constructed, which illustrate the dependency of the operating crack channelling mechanism and the corresponding critical crack channelling stress on the stiffness mismatch

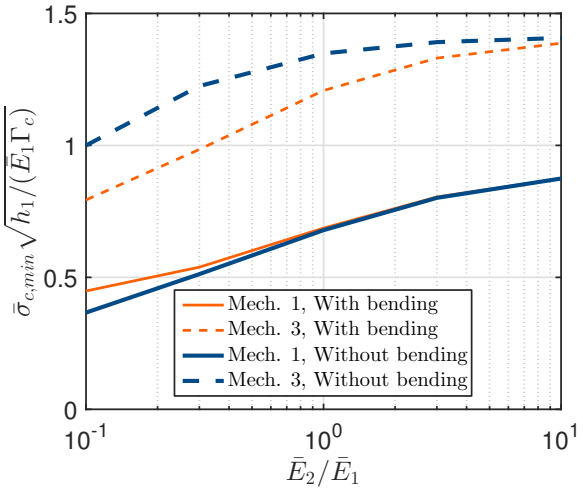

Figure 11: Critical channelling stress $\bar{\sigma}_{c,min}$ in the coating for *mechanism 1* (solid line) and *mechanism 3* (dashed line) as a function of the stiffness mismatch $\bar{E}_2/\bar{E}_1$. The orange thin lines and blue thick lines refer to bilayer systems *with bending* and *without bending*, respectively. In the normalization of the minimum channelling stress along the vertical axis, for *mechanisms 1* and *3* the toughness parameter is taken as $\Gamma_c = \Gamma_I$ and $\Gamma_c = \Gamma_d$, respectively. The results are computed for a relative layer thickness $h_2/h_1 = 10$, and are independent of the mismatch in coefficient of hygral expansion, $\bar{\beta}_2/\bar{\beta}_1$

between the layers and on the ratio between the interfacial toughness and coating toughness. Although the results are applicable to bilayers in a wide range of applications, the study focuses on the prediction of crack channelling in historical paintings. The effect of bending of the bilayer on crack channelling has been explored by comparing the fracture characteristics of the simply-supported, flexural bilayer with those of a rigidly supported bilayer studied in a previous work [23]. These two bilayer systems are representative of the different framing techniques used for historical paintings, with the simply-supported, flexural bilayer reflecting a regular wooden panel that can bend freely, and the rigidly supported bilayer characterizing a wooden panel that is fully constrained against a bending curvature by cradle additions composed of several horizontal members and corresponding orthogonal cross-pieces. A closed-form expression has been derived for the steady-state delamination stress of the flexural bilayer, which can be used to determine the critical moisture conditions that lead to crack channelling with unlimited delamination growth. Further, the failure mechanism maps constructed indicate that, independent of the type of framing technique applied, crack channelling with delamination can be prevented in historical paintings when the delamination toughness is larger than about half of the mode I toughness of the paint layer. Under these conditions paint flaking is avoided and the visual appearance of the painting is preserved. The failure maps constructed in this work may provide a useful tool for museum conservators to identify acceptable indoor humidity and temperature variations for which crack channelling with delamination remains absent in historical paintings.

A Remote stress distributions in coating and substrate

Figure 12 shows a doubly deflected crack in a brittle elastic coating of thickness h_1 that is connected to an elastic substrate of thickness h_2. Assume plane strain conditions, and that the bilayer is subjected to a uniform moisture content variation $\Delta\bar{m}$. The in-plane axial stresses that are induced in the coating (layer "1") and substrate (layer "2") by the moisture content variation follow from the hygro-elastic constitutive expressions as

$$\begin{aligned} \sigma_1(x,y) &= \bar{E}_1\left(\varepsilon_1(x,y) - \bar{\beta}_1\Delta\bar{m}\right) \ , \\ \sigma_2(x,y) &= \bar{E}_2\left(\varepsilon_2(x,y) - \bar{\beta}_2\Delta\bar{m}\right) \ , \end{aligned} \tag{23}$$

where $\bar{E}_i = E_i/(1-\nu_i^2)$ and $\bar{\beta}_i = \beta_i(1+\nu_i)$ are the plane-strain elastic modulus and hygroscopic coefficient of layer $i \in \{1,2\}$, respectively, and $\varepsilon_i(x,y)$ and $\bar{\beta}_i\Delta m(y)$ represent the total strain and hygroscopic strain, respectively. As illustrated in Figure 12, in the $x-y$ coordinate system adopted for describing the crack, the $x-$axis is located along the layer interface and the $y-$axis coincides with the crack symmetry axis located at the centre of the bilayer. The remote, moisture-induced layer stresses that govern the cracking process can be derived from force and moment equilibrium on an upstream cross-section remote from the crack, see also [37]. The upstream remote stresses in the coating and substrate may be formulated as $\sigma_1^\infty(y) = \sigma_1(x\to\infty, y)$ and $\sigma_2^\infty(y) = \sigma_2(x\to\infty, y)$, respectively. With these stresses, the net axial force and net moment on the upstream cross-section both vanish such that

$$\left\{ \begin{array}{l} \displaystyle\int_0^{h_1} \sigma_1^\infty(y)\mathrm{d}y + \int_{-h_2}^0 \sigma_2^\infty(y)\mathrm{d}y = 0 \ , \\ \displaystyle\int_0^{h_1} \sigma_1^\infty(y)y\mathrm{d}y + \int_{-h_2}^0 \sigma_2^\infty(y)y\mathrm{d}y = 0 \ . \end{array} \right. \tag{24}$$

Compatibility implies that the total axial strain is linear across the upstream cross-section of the bilayer such that

$$\varepsilon_i^\infty(y) = \kappa(y-y_n) \qquad \text{where} \qquad \varepsilon_i^\infty(y) = \varepsilon_i(x\to\infty, y) \qquad \text{with} \qquad i\in\{1,2\}\,, \tag{25}$$

in which κ is the curvature and y_n is the location of the neutral axis at the upstream cross-section. By inserting (25) into (23), and substituting the result into (24), κ and y_n can be solved as

$$\begin{aligned} \kappa &= \frac{6\bar{E}_1\bar{E}_2h_1h_2h(\bar{\beta}_2-\bar{\beta}_1)}{\bar{E}_1^2h_1^4+4\bar{E}_1\bar{E}_2h_1^3h_2+6\bar{E}_1\bar{E}_2h_1^2h_2^2+4\bar{E}_1\bar{E}_2h_1h_2^3+\bar{E}_2^2h_2^4}\,\Delta\bar{m}\ , \\ y_n &= -\frac{\bar{E}_1^2h_1^4\bar{\beta}_1+\bar{E}_2^2h_2^4\bar{\beta}_2+\bar{E}_1\bar{E}_2[4h_1h_2^3\bar{\beta}_1+4h_1^3h_2\bar{\beta}_2+3h_1^2h_2^2(\bar{\beta}_1+\bar{\beta}_2)]}{6\bar{E}_1\bar{E}_2h_1h_2h(\bar{\beta}_2-\bar{\beta}_1)}\ , \end{aligned} \tag{26}$$

with $h = h_1 + h_2$ the total thickness of the bilayer. Note from $(26)_2$ that for $\bar{\beta}_2/\bar{\beta}_1 < 1$ the neutral axis is located within the coating, $y_n > 0$, while for $\bar{\beta}_2/\bar{\beta}_1 > 1$ it is located in the substrate, $y_n < 0$. Inserting expressions (26) back into relations (25), followed by substituting the result into (23), provides the linear remote stresses in the coating and substrate as

$$\begin{aligned} \sigma_1^{\infty}(y) &= \bar{\sigma}_1 \left(1 - \frac{y}{h\zeta_1}\right) , \\ \sigma_2^{\infty}(y) &= \bar{\sigma}_2 \left(1 - \frac{y}{h\zeta_2}\right) , \end{aligned} \tag{27}$$

where

$$\begin{aligned} \bar{\sigma}_1 &= \frac{\bar{E}_1\bar{E}_2 h_2(\bar{\beta}_2 - \bar{\beta}_1)(\bar{E}_2 h_2^3 + 3\bar{E}_1 h_1^2 h_2 + 4\bar{E}_1 h_1^3)}{(\bar{E}_1^2 h_1^4 + 4\bar{E}_1\bar{E}_2 h_1^3 h_2 + 6\bar{E}_1\bar{E}_2 h_1^2 h_2^2 + 4\bar{E}_1\bar{E}_2 h_1 h_2^3 + \bar{E}_2^2 h_2^4)}\Delta\bar{m} , \\ \zeta_1 &= \frac{\bar{E}_2 h_2^3 + 3\bar{E}_1 h_1^2 h_2 + 4\bar{E}_1 h_1^3}{6\bar{E}_1 h_1 h^2} , \\ \bar{\sigma}_2 &= -\frac{h_1}{h_2}\omega\,\bar{\sigma}_1, \\ \zeta_2 &= -\frac{\bar{E}_1 h_1}{\bar{E}_2 h_2}\omega\,\zeta_1 , \end{aligned} \tag{28}$$

with the factor ω as

$$\omega = \frac{\bar{E}_1 h_1^3 + 3\bar{E}_2 h_2^2 h_1 + 4\bar{E}_2 h_2^3}{\bar{E}_2 h_2^3 + 3\bar{E}_1 h_1^2 h_2 + 4\bar{E}_1 h_1^3} . \tag{29}$$

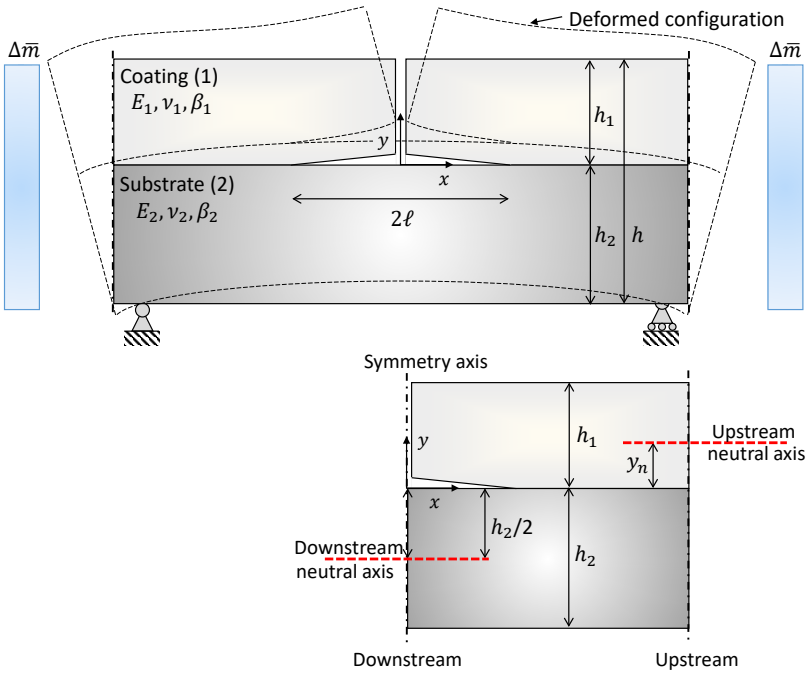

Figure 12: A doubly deflected crack in a coating-substrate system subjected to a uniform moisture content variation $\Delta\bar{m}$. In the figure it is assumed that $\bar{\beta}_2/\bar{\beta}_1 < 1$, as a result of which the neutral axis at the upstream cross-section remote from the crack is located within the coating, $y = y_n$. At the downstream cross-section the neutral axis is located halfway the substrate thickness, $y = -h_2/2$.

B Remote coating stress for steady-state delamination

For the doubly deflected crack sketched in Figure 12, delamination along the layer interface reaches a steady state when the delamination length tends to infinity, $\ell/h_1 \to \infty$ [23, 27–29, 37, 38]. Accordingly, the energy release rate G_d for interfacial delamination approaches an asymptotic value, $G_{d,ss} = G_d(\ell/h_1 \to \infty)$, which can be derived in closed form from the difference in elastic strain energy upstream and downstream of the delamination tip. From force equilibrium at the fractured, downstream cross-section at $x = 0$, the in-plane stress in the substrate appears to be zero, $\sigma_2^0(y) = \sigma_2(x = 0, y) = 0$. Hence, the steady-state energy release rate follows as

$$G_{d,ss} = \frac{1}{2}\int_0^{h_1} \sigma_1^{\infty}(y)\varepsilon_1^{e,\infty}(y)\mathrm{d}y + \frac{1}{2}\int_{-h_2}^{0} \sigma_2^{\infty}(y)\varepsilon_2^{e,\infty}(y)\mathrm{d}y \,, \tag{30}$$

where $\varepsilon_i^{e,\infty}(y)$ is the remote elastic strain in each layer $i \in \{1, 2\}$, upstream from the delamination tip. Inserting expressions (27) in Appendix A for the remote stresses $\sigma_1^{\infty}(y)$ and $\sigma_2^{\infty}(y)$, and invoking the constitutive relation $\sigma_i = \bar{E}_i\varepsilon_i^e$ for each layer $i \in \{1, 2\}$, equation (30) becomes

$$G_{ss} = \frac{1}{2}\frac{\bar{\sigma}_1^2 h_1}{\bar{E}_1}\left[1 - \frac{h_1}{\zeta_1 h} + \frac{h_1^2}{3\zeta_1^2 h^2} + \omega^2\frac{\bar{E}_1}{\bar{E}_2}\frac{h_1}{h_2}\left(1 + \frac{h_2}{\zeta_2 h} + \frac{h_2^2}{3\zeta_2^2 h^2}\right)\right] \,. \tag{31}$$

with the remote stress $\bar{\sigma}_1$ given by equation $(28)_1$ in Appendix A. Note that the subscript "d" has been omitted in equation (31), since the steady-state value is representative of *both* plane-strain delamination and crack channelling, i.e., $G_{ss} = G_d(\ell/h_1 \to \infty) = G_c(\ell/h_1 \to \infty)$, with G_c the energy release rate for crack channelling. Specifically, equality between the energy release rates for crack channelling and plane-strain delamination occurs at any point of the G_c versus ℓ/h_1 curve at which $\partial G_c/\partial\ell = 0$, whereby it turns out that this condition is met when $\ell/h_1 \to \infty$ [23, 25, 27, 30]. Progressive steady-state delamination occurs when the corresponding energy release rate G_{ss} equals the delamination toughness Γ_d, evaluated at the appropriate mode-mix $\Psi(\hat{l})$, i.e.,

$$G_{ss} = \Gamma_d(\Psi(\hat{l})) \,. \tag{32}$$

Inserting (31) into (32), the expression for the remote steady-state stress in the coating, $\bar{\sigma}_1 = \bar{\sigma}_{ss}$, becomes

$$\bar{\sigma}_{ss} = \left(2\bar{E}_1\Gamma_d\right)^{\frac{1}{2}}\left(h_1\left[1 - \frac{h_1}{\zeta_1 h} + \frac{h_1^2}{3\zeta_1^2 h^2} + \omega^2\frac{\bar{E}_1}{\bar{E}_2}\frac{h_1}{h_2}\left(1 + \frac{h_2}{\zeta_2 h} + \frac{h_2^2}{3\zeta_2^2 h^2}\right)\right]\right)^{-\frac{1}{2}} \,, \tag{33}$$

with the parameters ζ_1, ζ_2 and ω given by equations $(28)_2$, $(28)_4$ and (29) in Appendix A, respectively.

Acknowledgements

E.B. is grateful for the support by the Netherlands Organization for Scientific Research (NWO), Project 15873, “Engineering goes Beauty - A computational multi-physics modelling approach towards the preservation of historical oil paintings”, within the funding scheme “NWO Veni Award”. A.S.J.S. has received funding from the European Union’s Horizon 2020 research and innovation programme under grant agreement N. 814624. The authors would like to thank Matteo Rossi Doria from the *CBC Conservazione Beni Culturali Società Cooperativa* in Rome, Italy, and Paul van Duin from the *Rijksmuseum* in Amsterdam, the Netherlands, for providing images of historical panel paintings.

References

[1] M.A.J. Gils, van, P.J.J.H.A. Habets, G.Q. Zhang, W.D. van Driel, and P.J.G. Schreurs. Characterization and modelling of moisture driven interface failures. *Microelectronics Reliability*, 44(9-11):1317–1322, 2004.

[2] S.R. Choi, J.W. Hutchinson, and A.G. Evans. Delamination of multilayer thermal barrier coatings. *Mechanics of Materials*, 31(7):431 – 447, 1999.

[3] T.S. Hille, T.J. Nijdam, A.S.J. Suiker, S. Turteltaub, and W.G. Sloof. Damage growth triggered by interface irregularities in thermal barrier coatings. *Acta Materialia*, 57(9):2624–2630, 2009.

[4] B.F. Sørensen, H. Toftegaard, S. Linderoth, M. Lundberg, and S. Feih. Strength and failure modes of ceramic multilayers. *Journal of the European Ceramic Society*, 32(16):4165 – 4176, 2012.

[5] D.H. Timm, B.B. Guzina, and V.R. Voller. Prediction of thermal crack spacing. *International Journal of Solids and Structures*, 40(1):125 – 142, 2003.

[6] R. A. Luimes, A. S. J. Suiker, C. V. Verhoosel, A. J. M. Jorissen, and H. L. Schellen. Fracture behaviour of historic and new oak wood. *Wood Science and Technology*, 52(5):1243–1269, 2018.

[7] R.A. Luimes, A.S.J. Suiker, A.J.M. Jorissen, P.H.J.C. van Duin, and H.L. Schellen. Hygro-mechanical response of oak wood cabinet door panels under relative humidity fluctuations. *Heritage Science*, 6(72), 2018.

[8] F. Giorgiutti-Dauphiné and L. Pauchard. Painting cracks: A way to investigate the pictorial matter. *Journal of Applied Physics*, 120(6), 2016.

[9] M. Léang, F. Giorgiutti-Dauphiné, L.T. Lee, and L. Pauchard. Crack opening: from colloidal systems to paintings. *Soft Matter*, 13:5802–5808, 2017.

[10] M.F. Mecklenburg and C.S. Tumosa. Mechanical behavior of paintings subjected to changes in temperature and relative humidity. In M.F. Mecklenburg, editor, *Art in Transit: Studies in the Transport of Paintings*, pages 173–214, 1991.

[11] S. Bucklow. The description of craquelure patterns. *Studies in Conservation*, 42(3):129–140, 1997.

[12] Ł. Bratasz. Allowable microclimatic variations for painted wood. *Studies in Conservation*, 58(2):65–79, 2013.

[13] L. Krzemień, M. Łukomski, Ł. Bratasz, R. Kozłowski, and M.F. Mecklenburg. Mechanism of craquelure pattern formation on panel paintings. *Studies in Conservation*, 61(6):324–330, 2016.

[14] Ł. Bratasz and M.R. Vaziri Sereshk. Crack saturation as a mechanism of acclimatization of panel paintings to unstable environments. *Studies in Conservation*, 63(sup1):22–27, 2018.

[15] J. Crook and T.J.S. Learner. *The Impact of Modern Paints*. Tate Gallery Publishing, 2000.

[16] C.R.T. Young. Interfacial interaction of modern paint layers. In Thomas J.S. Learner, Patricia Smithen, Jay W. Krueger, and Michael R. Schilling, editors, *Modern Paints Uncovered Symposium*, pages 247–256, 2007.

[17] S. Tantideeravit, M.N. Charalambides, D.S. Balint, and C.R.T. Young. Prediction of delamination in multilayer artist paints under low amplitude fatigue loading. *Engineering Fracture Mechanics*, 112-113:41 – 57, 2013.

[18] J.D. Wood, C. Gauvin, C.R.T. Young, A.C. Taylor, D.S. Balint, and M.N. Charalambides. Cracking in paintings due to relative humidity cycles. *Procedia Structural Integrity*, 13:379 – 384, 2018.

[19] A. Brewer and C. Forno. Moiré fringe analysis of cradled panel paintings. *Studies in Conservation*, 42(4):211–230, 1997.

[20] E. O'Donoghue, A.M. Johnson, J. Mazurek, F. Preusser, M. Schilling, and M.S. Walton. Dictated by media: Conservation and technical analysis of a 1938 Joan Miró canvas painting. *Studies in Conservation*, 51(sup2):62–68, 2006.

[21] D. Daly Hartin and W. Baker. *Caring for paintings. Preventive conservation guidelines for collections.* Canadian Conservation Institute, https://www.canada.ca/en/conservation-institute/services/preventive-conservation/guidelines-collections.html.

[22] W.S. Elkhuizen, T.W.J. Callewaert, E. Leonhardt, A. Vandivere, Y. Song, S.C. Pont, J.M.P. Geraedts, and J. Dik. Comparison of three 3D scanning techniques for paintings, as applied to Vermeer's 'Girl with a Pearl Earring'. *Heritage Science*, 7(89), 2019.

[23] E. Bosco, A.S.J. Suiker, and N.A. Fleck. Crack channelling mechanisms in brittle coating systems under moisture or temperature gradients. *International Journal of Fracture*, 225:1–30, 2020.

[24] G. Gregori. Conservation and restoration of two wall painting fragments by Bernardino Luini. an intervention about frescoes torn and transferred on wooden boards and conserved in the Pinacoteca di Brera (Milan). Technical report, EGG 5, 2016.

[25] N.A. Fleck and L.G. Zhao. Microbuckle tunnelling in fibre composites. *Journal of the Mechanics and Physics of Solids*, 48(9):1865 – 1891, 2000.

[26] B.N. Cox and D.B. Marshall. Crack initiation in fiber-reinforced brittle laminates. *Journal of the American Ceramic Society*, 79(5):1181–1188, 1996.

[27] A.S.J. Suiker and N.A. Fleck. Crack tunneling and plane-strain delamination in layered solids. *International Journal of Fracture*, 125(1):1–32, 2004.

[28] A.S.J. Suiker and N.A. Fleck. Modelling of fatigue crack tunneling and delamination in layered composites. *Composites Part A: Applied Science and Manufacturing*, 37(10):1722 – 1733, 2006.

[29] J.W. Hutchinson and Z. Suo. Mixed mode cracking in layered materials. In J.W. Hutchinson and T.Y. Wu, editors, *Advances in Applied Mechanics*, volume 29, pages 63–191. Academic Press, New York, 1992.

[30] J.L. Beuth. Cracking of thin bonded films in residual tension. *International Journal of Solids and Structures*, 29(13):1657 – 1675, 1992.

[31] J.W. Hutchinson, M.E. Mear, and J.R. Rice. Crack paralleling an interface between dissimilar materials. *ASME Journal of Applied Mechanics*, 54(4):828–832, 1987.

[32] J.R. Rice. Elastic fracture mechanics concepts for interfacial cracks. *ASME Journal of Applied Mechanics*, 55:98–103, 1988.

[33] J. Dundurs. Edge-bonded dissimilar orthogonal elastic wedges. *ASME Journal of Applied Mechanics*, 36:650–652, 1969.

[34] J.R. Rice. A path independent integral and the approximate analysis of strain concentration by notches and cracks. *ASME Journal of Applied Mechanics*, 35(2):379–386, 1968.

[35] Ł. Bratasz, K.G. Akoglu, and P. Kekicheff. Fracture saturation in paintings makes them less vulnerable to environmental variations in museums. *Heritage Science*, 8(11), 2020.

[36] B. Rachwał, Ł. Bratasz, L. Krzemien, M. Łukomski, and R. Kozłowski. Fatigue damage of the gesso layer in panel paintings subjected to changing climate conditions. *Strain*, 48(6):474–481, 2012.

[37] P.J.J. Forschelen, A.S.J. Suiker, and O. van der Sluis. Effect of residual stress on the delamination response of film-substrate systems under bending. *International Journal of Solids and Structures*, 97-98:284–299, 2016.

[38] L.B. Freund and S. Suresh. *Thin film materials. Stress, Defect formation and Surface evolution.* Cambridge University Press, Cambridge, United Kingdom., 2004.